Experiments in Fluids 33 (2002) 443–457
DOI 10.1007/s00348-002-0474-z

A generalized processing technique in digital particle image velocimetry with direct estimation of velocity gradients

S. Mayer

Abstract A technique is proposed for the processing of digital particle image velocimetry (PIV) images, in one single step providing direct estimates of fluid velocity, out-of-plane vorticity and in-plane shear rate tensor. The method is based on a generalization of the standard PIV cross-correlation technique and substitutes the usual discrete cross-correlation of image pairs with a correlation of interpolated two-dimensional image intensity functions, being subject to affine transformations. The correlation is implemented by using collocation points, on which image intensity values are interpolated. The resulting six-dimensional correlation function is maximized using a general purpose optimization algorithm. The use of the method is demonstrated by application to different types of synthetically generated image pairs constructed with known particle displacement functions. The resulting errors are assessed and compared with those of a representative standard PIV method as well as with those of the present technique using no differential quantities in the search of the peak location. The examples demonstrate that significant improvements in accuracy can be obtained for flow fields with regions containing strong velocity gradients.

1 Introduction

The basic principle of particle image velocimetry (PIV) and particle tracking velocimetry (PTV) is simple and has been used for decades in studies of moving objects. The tracer commonly used in PIV/PTV is particles which are sufficiently small to accurately follow the local flow. By acquisition of two exposures with a known time separation, the velocity can be inferred from particle image displacements. In general, two types of processing of the image pairs can be distinguished: in PTV, individual particles are identified on subsequent images and the particle displacements are directly geometrically measured. While this is feasible for low particle concentrations, the correspondence problem of identifying individual particles in either image becomes increasingly difficult with higher particle densities. However, extensive research is still being carried out to solve those problems, since the promise of PTV is ultimately to provide the maximum spatial resolution of the underlying velocity field.

The alternative processing approaches have collectively been termed correlation image velocimetry (CIV) (Fincham and Spedding 1997), all inferring the transport of particles or passive scalar field from correlation analysis. Since no individual tracer has to be identified and the analysis relies on a statistical basis, such processing can be made rather robust. The well-known standard cross-correlation PIV technique is one example of such CIV techniques. Here, each of two subsequent images is decomposed into sub-images of the order of 10–100 px in size, the so-called interrogation windows. For every window from the two images, a velocity estimate is made on the basis of their mutual cross-correlation. Because only one velocity vector is provided for every window pair, the achieved spatial resolution will usually be somewhat lower than ultimately achievable in PTV. In recent years, extensive work has been carried out to estimate the errors in CIV-based methods and to identify their sources (see e.g., Nogueira et al. 1997; Huang et al. 1997; Fouras and Soria 1998; Westerweel 2000). Further, many suggestions have recently been made on how to improve both the accuracy of PIV and its spatial resolution.

One well-known major problem in standard PIV stems from the fact that the processing algorithm assumes the velocity field to be constant throughout the window. However, if velocity gradients are present in the field, they will broaden and lower the cross-correlation peak, generally adding errors to the peak location estimate and therefore reducing the accuracy of the measured mean velocity within that window. It seems common to most attempts at improving the ability of PIV to accurately measure strained flow fields that the techniques fundamentally still rely on the basic discrete cross-correlation technique for the estimation of the displacement vectors within an interrogation window. The improvements are

Received: 2 March 2001 / Accepted: 16 April 2002
Published online: 4 July 2002

S. Mayer (✉)
Informatics and Mathematical Modelling,
Technical University of Denmark, 2800 Lyngby, Denmark
E-mail: stm@mek.dtu.dk

This work was financed by the Danish Technical Research Council (STVF grant 9801635). Their support is greatly appreciated. I should like to thank Dr. U. Ullum for making available the PIV image pairs and for discussion on fundamentals in PIV processing. I am grateful to Assoc. Prof. H.B. Nielsen and his co-workers for making available to me the optimization algorithms used in the present work and for valuable discussions on the use of those methods. Further, thanks to Assoc. Prof. K.E. Meyer and Prof. P.S. Larsen for valuable comments. Finally I should like to express my gratitude to the reviewers for their suggestions, which lead to considerable improvements in the paper.

generally sought by applying various post- and/or pre-processing techniques to the data. In particular, window shifting and distortion have been used to reduce the in-plane loss of particles and counteract the broadening of the correlation peak.

Seemingly independent of the efforts in PIV, Tokumaru and Dimatakis (1995), Merkel et al. (1996), Deusch et al. (2000) and others have employed generalized pattern matching techniques from general image analysis to infer velocity fields from the evolution of a transported tracer scalar field. In those attempts, a generalized correlation function between a sequence of images is maximized by various optimization techniques. In contrast to PIV, the equations of motion of the fluid and also certain smoothness restrictions are added as constraints in the search for a global image transformation function.

It is the author's impression that, while the efforts in both classic PIV and generalized pattern matching have contributed to very substantial improvements in the techniques, they have also added to the complexity of the processing algorithms in use. With this background, the aim of the present study has been to reformulate the fundamental PIV processing technique by means of general techniques from image analysis and pattern matching algorithms without sacrifice to the conceptual simplicity of the cross-correlation-based PIV processing. The method directly searches for the optimum displacement and displacement gradient, maximizing a generalized correlation function defined locally in the image. At the same time, window shifting and distortion are integrated into the interrogation procedure, making iterative processing sweeps and numerical computation of displacement derivatives in the image field unnecessary.

Although the present starting point is close to that of, for example, Tokumaru and Dimatakis (1995), the proposed method is conceived and implemented as a generalization of the standard cross-correlation PIV processing technique. Therefore, the present outline takes its starting point in a general description of the fundamentals of two-frame PIV analysis and in a discussion of some relevant details.

1.1 Standard approach

The basic methodology of PIV has been established for many years now, see the text of Raffel et al. (1998) for a comprehensive description. In the following, the standard analysis of a particle image pair I_1,I_2 is considered, each image being represented as a two-dimensional array of pixel values

$$I_1 = \mathrm{fct}(i,j), \quad I_2 = \mathrm{fct}(i,j) \tag{1}$$

at the corresponding instants t_1 and t_2. The PIV methodology is based on the assumption that a shifting transformation in the image index space

$$S_{u,v}(i,j) = (i+u,\ j+v) \tag{2}$$

can be used to bring one image close to the other locally within a given interrogation window A,

$$I_1\left[S_{u,v}(i,j)\right] \approx I_2(i,j) \quad \text{for } (i,j) \in A, \tag{3}$$

where the integer displacement vector (u, v) is an approximation to the particle displacement vector projected onto the image plane. The cross-correlation of the shifted first image with the second image is defined as

$$G(u,v) = C\{I_1\left[S_{(u,v)}(i,j)\right] I_2(i,j)\}, \tag{4}$$

where C is the correlation operator

$$C(I_1,I_2) = \frac{1}{N}\sum_{(i,j)\in A}[I_1(i,j)][I_2(i,j)], \tag{5}$$

with N the number of pixels in the window.

In order to estimate the particle displacement, the location of the maximum value of $G(u, v)$ is found

$$(u,v) \approx \arg\max_{(u,v)\in T} G(u,v), \tag{6}$$

where T is the domain of relevant possible integer shifting parameters (u, v). Usually, Fourier transformation is employed together with the Convolution theorem to compute

$$G(u,v) = FT^{-1}[FT(I_1)FT(I_2)], \tag{7}$$

since Eq. 7 can be evaluated considerably more efficiently by use of fast Fourier transform (FFT) algorithms than by evaluating the sum in Eq. 4 directly, if $G(u, v)$ is needed for all $(u, v) \subset T$.

Being important in the evaluation of the proposed new method, a number of aspects of the above "standard method" should be noted.

The shifting operator S acts as a model for the displacement within an interrogation window and can be viewed as a zeroth order Taylor approximation, as pointed out for example by Tokumaru and Dimatakis (1995). Thus, as mentioned before, it is a premise of the above method that the displacement field which carries particles in image I_1 to their corresponding locations in I_2 is approximately constant throughout the interrogation window A. Otherwise the correlation peak broadens, making an accurate identification of the maximum more difficult. The direct way to overcome this problem is obviously to minimize the interrogation window size, thereby minimizing the velocity differences within the window. However, for interrogation window sizes comparable in size with particle displacements, a considerable number of particles present in the window of the first image have moved out of the corresponding window of the second image and vice versa. This so-called in-plane loss of particles can be accounted for by shifting the window location from one image to the other parallel to the displacement vector; see the text of Raffel et al. (1998) or the papers by Westerweel et al. (1997), Scarano and Riethmuller (1999) and others. The window-shifting technique has been shown to be crucial and has readily been implemented in most PIV analysis algorithms today. The window offset is usually determined on the basis of an initial standard PIV interrogation.

In order to deal with the degradation of the correlation peak in the presence of displacement gradients, Huang et al. (1993, 1998), Jambunathan et al. (1995), Nogueira et al. (1999) and Lin and Perlin (1998) have extended the window-shifting operation also to involve rotation and

deformation of the second window. In this so-called particle image distortion (PID) technique, velocity gradients are estimated by a standard PIV technique and then used to distort the particle images. Those preprocessed images are then again analyzed by a standard PIV method, the whole procedure optionally being repeated several times. Huang et al. (1993) demonstrated that considerable improvements in accuracy and robustness of the measurements could be gained by this method. However, stability problems have been encountered when employing image distortion repeatedly, a problem which can be cured by using weighting functions in the image cross-correlation function (Nogueira et al. 1999). For a recent review on multi-scan methods, see Scarano and Riethmuller (2000).

The standard analysis is performed in the discrete pixel space (i, j). Sub-pixel resolution is usually sought by employing interpolation techniques around the maximum peak of $G(u, v)$. Although such interpolation in favorable circumstances has been shown to improve accuracy dramatically, velocity estimates usually tend to contain bias errors towards the nearest integer displacement value. This phenomenon, termed peak-locking, has been the subject of extensive work and testing. For a theoretical analysis of the achievable sub-pixel accuracy, see Westerweel (2000).

Since the interrogation window is a subset of the discrete image, it most often has a rectangular (usually quadratic) shape. Since FFT-based correlation algorithms are almost always employed, window sizes of 2^n px are usually used. However, Gui and Merzkirch (1998) have described ways of overcoming these restrictions with no or little penalty in computational efficiency.

2 Generalized method

2.1 Fundamentals

2.1.1 The shifting operator

The new method we propose in the present study takes its starting point in the transformation of the discrete images $I_1(i, j)$ and $I_2(i, j)$ at the corresponding instants t_1 and t_2 to their continuous counterparts $F_1(x, y)$, $F_2(x, y)$ by use of a given interpolation algorithm Q:

$$F_1(x,y) = Q(I_1, x, y) \tag{8}$$

$$F_2(x,y) = Q(I_2, x, y) \tag{9}$$

All of the following analysis is now carried out in the continuous space of (x, y).

The shifting operator S is extended to the continuous affine transformation operator

$$S_{u,v,w,s_{ij}}(x,y) = \begin{bmatrix} u \\ v \end{bmatrix} + \begin{bmatrix} s_{11} & s_{12}-\omega \\ s_{12}+\omega & s_{22} \end{bmatrix} \begin{bmatrix} x-x_c \\ y-y_c \end{bmatrix} \tag{10}$$

defining linear movement (by u and v), rotation (by ω), and linear deformation (by the deviatoric strain tensor s_{ij}, being symmetric, $s_{ij}=s_{ji}$) around the window center point (x_c, y_c).

This represents a first-order Taylor expansion of the displacement field around the center point. In an alternative formulation, the rotation parameter ω could have been omitted and rotation could instead have been included within a non-symmetric gradient:

$$\begin{bmatrix} g_{11} & g_{12} \\ g_{21} & g_{22} \end{bmatrix} = \begin{bmatrix} s_{11} & s_{12}-\omega \\ s_{12}+\omega & s_{22} \end{bmatrix} \tag{11}$$

the two formulation being exactly equivalent. The reason for storing rotation and deviatoric deformation separately is both conceptual and convenient for testing purposes, allowing the individual types of window motion/distortion to be switched on and off. In the following, the parameters (u, v, s_{ij}) will be denoted

$$q = \left(u, v, \omega, s_{11} s_{22,} s_{12}\right) \tag{12}$$

for brevity.

2.1.2 Interrogation

Given a virtual point $p_h = (x_h, y_h)$ at time $t_h = \frac{t_1+t_2}{2}$ halfway between the recording instants t_1 and t_2, undergoing the transformation S_q within the interval from t_1 to t_2, the corresponding locations of this point at the start and end of the interval, t_1 and t_2 are

$$p_1 = (x_1, y_1) = S_{-\frac{1}{2}q}(p_h), \tag{13}$$

$$p_2 = (x_2, y_2) = S_{\frac{1}{2}q}(p_h), \tag{14}$$

respectively. A virtual interrogation area A at instant t_h is now constructed covering the virtual images of particles at that instant. According to the transformation S_q, particle image patterns

$$Q\left[I_1, S_{-\frac{1}{2}q}(x_h, y_h)\right] \tag{15}$$

$$Q\left[I_2, S_{\frac{1}{2}q}(x_h, y_h)\right] \tag{16}$$

are then constructed for the instants t_1 and t_2.

Analogously to the standard approach a cross-correlation function between those patterns is considered:

$$G(q) = C\left[Q\left(I_1, S_{-\frac{1}{2}q}(x_h, y_h)\right), \quad Q\left(I_2, S_{\frac{1}{2}q}(x_h, y_h)\right)\right], \tag{17}$$

where C denotes a continuous correlation operator of the continuous image functions over a virtual interrogation area $(x_h, y_h) \subset A$,

$$C(F_1,F_2) = \frac{\int_A [w(r)F_1(x,y)][w(r)F_2(x,y)]\mathrm{d}A}{\sqrt{\int_A w(r)[F_1(x,y)]^2\mathrm{d}A \int_A w(r)[F_2(x,y)]^2\mathrm{d}A}} \tag{18}$$

C is by definition bounded to $-1 \le C \le 1$ for any set of intensity functions F_1 and F_2. $w(r)$ defines a weight function, with r denoting the distance from the window center point

$$r=\sqrt{(x-x_c)^2+(y-y_c)^2}, \tag{19}$$

with w=0 at the boundary of A, ensuring C to be a reasonably smooth function of q. Similarly to the standard approach, the method now seeks to find the closest match between two shifted continuous pattern functions by finding the cross-correlation peak within the parameter space of q,

$$q_{\text{opt}}=\arg\max_{q}[G(q)]. \tag{20}$$

For practical applications, the cross-correlation $G(q)$ must be approximated with a corresponding discretized version. Further, the evaluation of $G(q)$ for a large number of parameters sets $q=(u,v,s_{11},s_{22},s_{12})$ giving good coverage of the six-dimensional parameter space is not feasible computationally. Therefore, Eq. 20 is treated as a generic optimization problem, which is sought to be solved by a general optimization code. Since optimization algorithms are usually constructed for finding minima, Eq. 20 is reformulated to

$$q_{\text{opt}}=\arg\min_{q}[1-G(q)], \tag{21}$$

2.2 Implementation

In the preliminary implementation for the present study, the conversion of the pixelized images to continuous two-dimensional functions is performed by employing the simplest and cheapest possible method still giving continuous functions F_1, F_2, which is piecewise bilinear interpolation,

$$\begin{aligned} Q(I,x,y) = {} & (1-\varepsilon_x)(1-\varepsilon_y)I(i,j) \\ & + (1-\varepsilon_x)\varepsilon_y I(i,j+1) \\ & + \varepsilon_x(1-\varepsilon_y)I(i+1,j) \\ & + \varepsilon_x\varepsilon_y I(i+1,j+1) \end{aligned} \tag{22}$$

with

$$\varepsilon_x = x-i, \quad \varepsilon_y = y-j \tag{23}$$

and i, j chosen so that $x\subset[i,i+1]$ and $y\subset[j,j+1]$, respectively.

In order to numerically compute cross-correlations between the two particle image patterns, a finite set of discrete collocation points $p_i=(x_h,y_h)_i$ is chosen. For symmetry, the interrogation window A is taken to be the area within a circle of radius R, and the collocation points are located with an average distance to nearest neighbors of about 1 px width (see Fig. 1). Any closer coverage would not contribute any additional information. Since every collocation point roughly covers an area of 1 px^2, the total number of points N is approximately

$$N \approx \pi R^2. \tag{24}$$

The correlation operator C in Eq. 18 is substituted with the discretized version

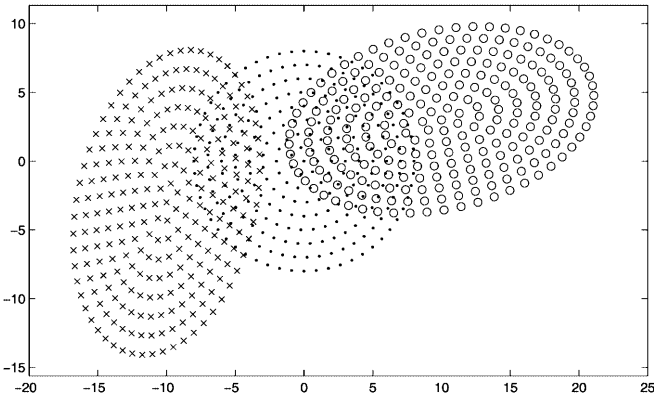

Fig. 1. Interrogation collocation points for window size $2r$=16: ·, collocation points at $t_h=\frac{t_1+t_2}{2}$; ×, collocation points at t_1, having undergone the transformation $S_{-\frac{1}{2}q}$; ○, collocation points at t_2, having undergone the transformation $S_{\frac{1}{2}q}$

$$C(F_1,F_2)=\frac{\Sigma_i\{[w(r_i)]^2F_1(x_i,y_i)F_2(x_i,y_i)\}}{\sqrt{\Sigma_i\{w(r_i)[F_1(x_i,y_i)]^2\}\Sigma_i\{w(r_i)[F_2(x_i,y_i)]^2\}}} \tag{25}$$

again by definition ensuring $-1 \le C \le 1$. The weight function w is chosen to be parabolic for simplicity

$$w(r)=1-\left(\frac{r}{R}\right)^2, \tag{26}$$

and the optimization problem is stated as

$$q_{\text{opt}}=k^{-1}\arg\min_{kq}[1-G(kq)] \tag{27}$$

with

$$G(kq)=C\left\{F_1\left[S_{-\frac{1}{2}kq}(x,y)\right], \quad F_2\left[S_{\frac{1}{2}kq}(x,y)\right]\right\} \tag{28}$$

The individual terms within the summation of Eqs. 25 and 28 are evaluated by shifting every point (x_i,y_i) according to $\pm kq/2$ and then interpolating within the images F_1, F_2, respectively, using Eq. 22. Being important for ensuring an optimization problem as well- conditioned as possible, the diagonal matrix

$$k=\text{diag}(1,1,R,R,R,R) \tag{29}$$

is introduced in order to scale all arguments in the optimization problem to approximately the same order of magnitude. To prevent the optimization algorithm requiring values of G for arguments kq outside the relevant parameter space, such as the sampling of F outside the image index space, the following constraint is introduced:

$$\|kq\|_2 < P, \tag{30}$$

where P is an upper bound of the displacement, estimated a priori.

For solving the optimization problem, Eq. 27, the iterative method VF13AD by Powell (1982), is chosen and applied in an implementation (MINCF) of Madsen et al. (1990). At every iteration step, the method requires for one

parameter set kq the value $G(kq)$ and its Jacobian $\frac{\partial G(kq)}{\partial kq}$, which is approximated by finite differences, requiring six additional evaluations of $G(kq)$. The step size used for the finite difference approximation was chosen to be 10^{-6} px. Throughout the work, the accuracy of the peak location was required to be less than 10^{-5}px. The necessary starting guess for the optimization algorithm is computed by extrapolation from found sets q_{opt} of neighbor windows.

The above method was implemented using the software package MATLAB (The Mathworks Inc., http://www.mathworks.com/) and its image tool box. All computations are carried out within MATLAB, except for the evaluation of $G(kq)$ and $\frac{\partial G(kq)}{\partial kq}$, which for computational efficiency was performed in a compiled C-subroutine called by the MATLAB program.

3
Validation test results

In the following, an attempt is made to demonstrate and investigate the properties of the present method by testing on different image pairs. In particular, the following two aspects will be addressed:

- How accurate can the magnitude of a constant displacement field be inferred on a sub-pixel level? The testing will roughly follow a track similar to that of Huang et al. (1997).
- Is the new method an improvement with respect to velocity measurements in sheared flows? The method is tested on two different synthetic image pairs, which are constructed on the basis of known displacement distributions, allowing exact comparisons.

Regarding the synthetic image pairs, the main variables which are varied in the following investigation are the interrogation window size and the particle image size, while the particle density is kept constant.

For all test cases, the following methods are applied and compared.

- (A) As a representative of the current standard PIV processing techniques, the MATLAB-based package MatPIV v. 1.4 (Jensen et al. 2001) is employed in its default state. In the following, it is referred to as the standard method. MatPIV closely follows the recommendations made by Raffel et al. (1998). It uses a multi-scan procedure, the first sweep defining the interrogation window displacement for the next sweeps. MatPIV employs an FFT-based algorithm for the cross-correlation and uses Gaussian interpolation for the sub-pixel estimation of the cross-correlation peak. Further, outliers are found by local median filtering and interpolated by the use of neighbor vectors. MatPIV is generally employed for interrogation window widths of $2R$=16 px, 32 px and 64 px.
- (B) The new method, but using optimization of the linear displacement (u,v) only and not including rotation and shear, $\omega=s_{ij}=0$. Interrogation window diameters used are $2R$=16, 24, 32, 40, 48, 64, 80, 96 px with the corresponding numbers of collocation points, N=253, 547, 953, 1,471, 2,101, 3,697, 5,741, 8,233, respectively.
- (C) The new method, employing optimization of all six degrees of freedom in q. The interrogation window diameter and corresponding numbers of collocation points are the same as for B.

While the MatPIV package is used in its default state as explained in A, in approaches B and C neither pre- nor post-processing of the data is performed unless specifically stated.

3.1
Constant displacement field

The natural starting point for evaluating the new method is obviously to test its ability to measure a constant displacement field within sub-pixel accuracy, and to measure the resulting bias (peak-locking effect) and random error levels as functions of window size $2R$, particle image size d_p and particle displacement d_t.

The investigation is substantially simplified using arguments similar to those of Westerweel (1997) and Huang et al. (1997) due to the fact that the collocation points are shifted in either image. Suppose the particle displacement is written as $d_t=n_t+\epsilon_t$ the error of the measured displacement is a function of ϵ_t only. Hence it is sufficient to analyze the errors within the displacement interval $0 < d_t <= 0.5$.

Synthetic images are created by randomly distributing particles over the image plane of 1,024×1,024 px^2 with an average density of 0.0195 l/px^2, giving on average five particles to an interrogation window of width 16×16 px^2 and 20 particles to a window of 32×32 px^2. Every particle is projected onto the discrete images with a Gaussian bell intensity distribution of fixed size d_p=1.5, 2, 3, 4, 6 px. The particles are translated a distance d_t in the x-direction and then projected similarly onto a second image. The images are processed with all three methods with a step size between neighbor interrogation windows of Δ=16 px. The resulting estimated displacement fields (u, v) are then analyzed statistically.

Outliers are detected by restricting vectors to be within three standard deviations from the mean. Since the package MatPIV relies on its own outlier analysis and removal procedure, only a few outliers are removed additionally to those already removed by MatPIV. In the optimization procedures, the outlier rate is higher, in particular when using the optimization approach including gradients (Method C) in cases with small particle image sizes and small interrogation windows.

For the following analysis, the detected outliers are removed. The remaining vectors are then analyzed in terms of mean and rms values of the displacement error u–d_t, $E(u–d_t)$ and $\sigma(u–d_t)$, respectively. As can be expected, the mean error $E(u–d_t)$ proves to be independent of the interrogation window size for all three methods. It can be shown directly by symmetry considerations that the mean error is identically zero for both d_t=0 and d_t=0.5 px due to the window shifting. Figure 2 shows the mean error within the interval $0 \le d_t \le 0.5$ px for different particle image sizes for Method C. The bias errors of Method B are virtually indistinguishable from those of Method C, which is to be expected due to the absence of velocity gradients.

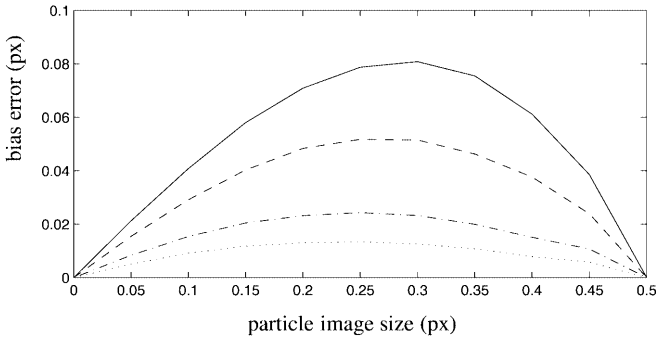

Fig. 2. Method C, optimization of $q=(u, v, \omega, s_{ij})$ on synthetic PIV-image pair with constant displacement. Bias error as function of particle sub-pixel displacement: —, particle image diameter d_p=1.5 px; - - -, d_p=2 px; ·–·, d_p=3 px; · · ·, d_p=4 px

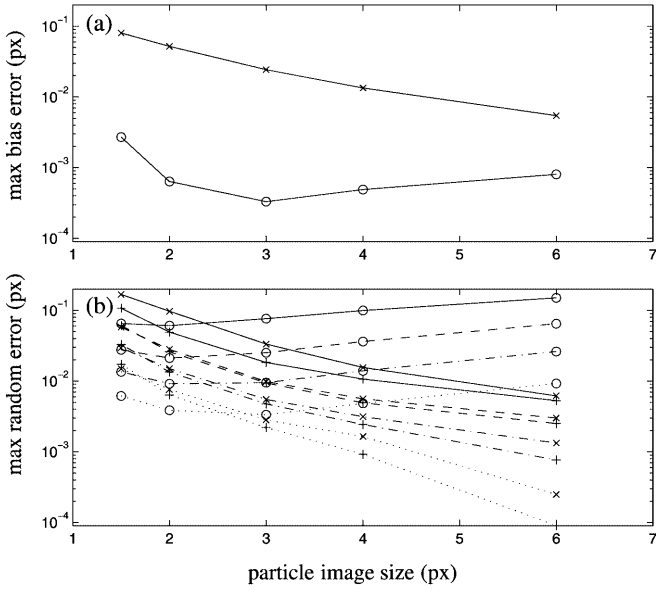

Fig. 3a, b. Synthetic PIV-image pair with constant displacement: **a** max bias error; **b** max random error for different interrogation window sizes as a function of particle image size d_p. ○, Method A; +, Method B; ×, Method C; —, $2R$=16 px, - - -, $2R$=32 px; ·–·, $2R$=64 px; · · ·, $2R$=128 px

Figure 3 shows the maximum bias error made within $0 \le d_t \le 0.5$ for both Method C and Method A. The Gaussian sub-pixel interpolation of the standard method essentially removes all peak-locking effects for all particle image sizes tested, while in comparison the optimization techniques show quite significant peak-locking, which worsens with decreasing particle image size.

The random error levels, $\sigma(u–d_t)$, generally appear to be largest for d_t=0.5 for all three methods. Figure 3b shows the random error level at d_t=0.5 for different interrogation sizes as function of particle image size. In all cases, noise levels are reduced with increasing interrogation window size, as expected. The optimization approaches (Methods B and C) produce decreasing noise levels for increasing particle image size, in all cases Method B doing somewhat better than Method C. In contrast, the noise error levels produced by the standard approach increase slightly with the particle image size. For small particle sizes, the MatPIV package produces fewer random errors than the optimization approaches, while for larger particles the opposite is the case.

3.2 Irrotational oscillatory displacement field

The second test is performed to investigate how spatially periodic structures are resolved. A synthetic image pair is created with randomly distributed particles with the same density of 0.0195 l/px^2 as before. The particles are then displaced according to the irrotational oscillatory displacement field

$$u_x(x,y) = A\cos\left(\frac{2\pi x}{\lambda}\right)\sin\left(\frac{2\pi x}{\lambda}\right),$$
$$u_y = A\sin\left(\frac{2\pi x}{\lambda}\right)\cos\left(\frac{2\pi y}{\lambda}\right), \qquad (31)$$

where λ is the wavelength, and A the amplitude. Again particles are projected onto either image with Gaussian intensity distributions, the sizes chosen to be d_p=2 px and d_p=4 px.

Two different values for amplitude A were chosen. For case A=1, the spatial resolution of the methods is tested without introducing significant broadening of the correlation peaks for small interrogation windows. In the second case, A=5, the methods' ability to deal with non-constant particle displacements within a window is brought to test, since it features a maximum displacement gradient of about 25%.

The images are processed by all three methods, with a step size between neighbor interrogation windows of Δ=8 px. The resulting vector fields are decomposed into a number of subdomains of 8×8 vectors, each of which covers one wavelength λ=128 px in either direction. The subsequent averaging across points of equivalent phase in the subdomains then provides phase-averaged displacements $E_{ph}(u_x)$ and $E_{ph}(u_y)$ and their respective rms values $\sigma_{ph}(u_x)$ and $\sigma_{ph}(u_y)$.

Figure 4 shows normalized velocity profiles of $E_{ph}(u_x)$ along the line x = 0, as they are estimated by the different methods in the case of d_p = 4 px. For the small amplitude case, A = 1 px, the bias errors of all three methods prove to be comparable for the small window sizes, $2R$ = 16 and 32 px, while for larger windows, Method C has the smallest bias. However, when the interrogation window covers one wavelength, $2R = \lambda$, neither of the three methods at test is obviously able to resolve the displacement field, the result being weighted spatial averages close to zero. In the case of large wave amplitude, A = 5 px, Method B generally produces too many outlier vectors to allow reliable estimation of velocity profiles at all, its robustness even weakening with decreasing particle size. Also Method A produces many outliers, most of which are removed and interpolated by the MatPIV package itself. However, Methods A and C provide satisfactory results for the case A = 5 px. Both methods resolve the oscillatory field satisfactorily for small window sizes ($2R$ = 16), but for larger windows, Method C produces significantly less bias error than A, which tends to chop the oscillation peak. Another qualitative feature shown in Fig. 4 is the symmetry of the

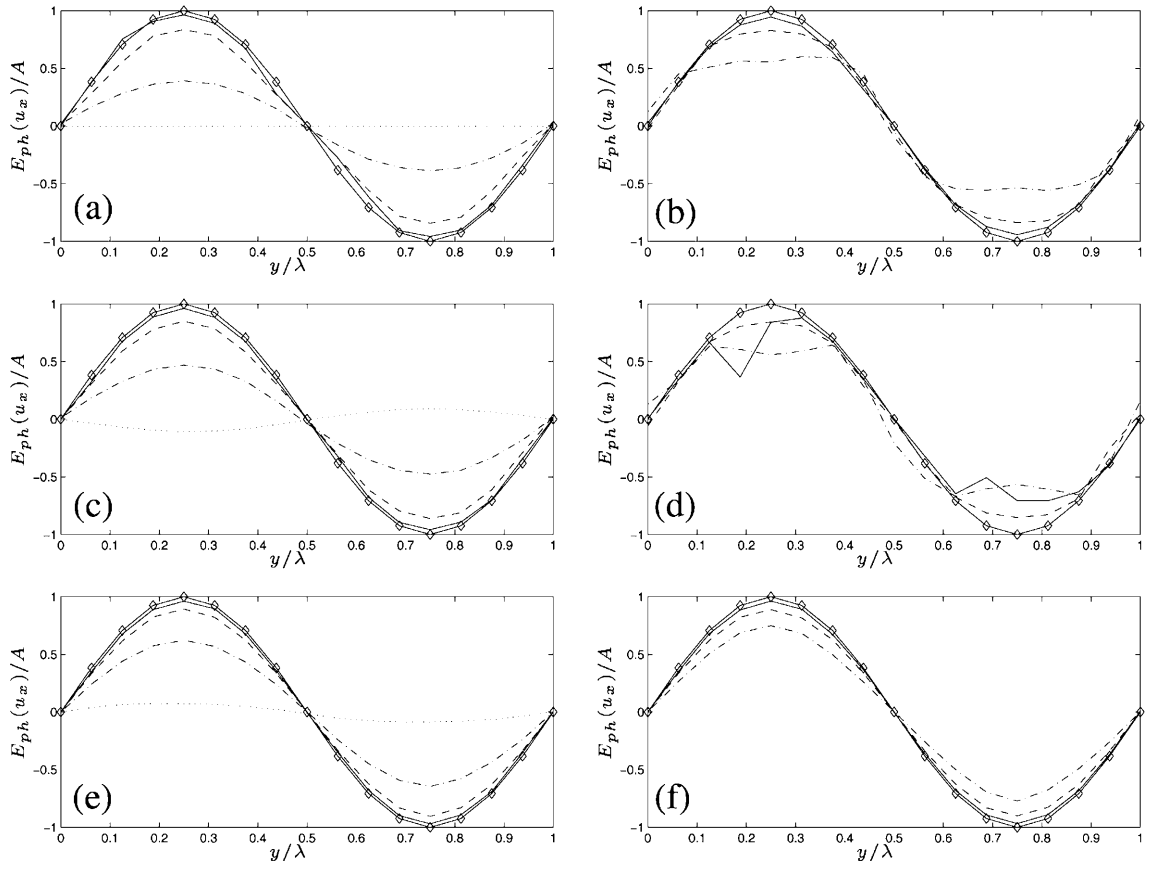

Fig. 4a–f. Synthetic PIV-image pair with periodic irrotational displacement field, Eq. 31 with particle image size d_p=4 px. Phase-averaged velocity component $E_{ph}(u_x)/A$ along line x=0: **a** Method A, A=1 px; **b** Method A, A=5 px; **c** Method B, A=1 px; **d** Method B, A=5 px; **e** Method C, A=1 px; **f** Method C, A=5 px; *diamonds*, exact profile; —, 2R=16 px; - - -, R=32 px; ·–·, 2R=64 px; ···, 2R=128 px

profiles. Methods B and C reproduce the symmetry of the profiles, while Method A tends to give a spatial shift.

Figure 5 shows the corresponding profiles of $\sigma_{\mathrm{ph}}(u_x)$ along of the line x = 0. For the case A = 1 px, Method C features rms levels on average about five times lower than those of Methods A and B. In the case A = 5 px, the difference is about one order of magnitude. Moreover, a distinct difference in the shape of the rms profiles can be seen for larger window sizes. Method C shows its highest random errors at displacement peak locations, while in Methods A and B the noise is largest at locations where the displacement gradients have their maximum.

Figure 6 directly compares the mean bias error

$$\frac{1}{A\lambda^2}\int_0^{\lambda}\int_0^{\lambda}\left|E_{\mathrm{ph}}(u_x)-u_x^{\mathrm{exact}}\right|\mathrm{d}x\,\mathrm{d}y \tag{32}$$

and mean random

$$\frac{1}{A\lambda^2}\int_0^{\lambda}\int_0^{\lambda}\sigma_{\mathrm{ph}}(u_x)\mathrm{d}x\,\mathrm{d}y, \tag{33}$$

of the x displacement measured by the methods as a function of interrogation window size 2R, for the particle image sizes d_p=2 px and 4 px and amplitudes A=1 px and 5 px. Method C generally performs better in comparison with the other methods tested. For all methods, some dependency of the bias errors on the particle image size is detected. The mean random errors of Method C are seen to be clearly smaller than those of the other methods, this being especially pronounced for case A=5 px. Generally, for all methods, random errors are reduced with increasing particle image size.

The divergence of Eq. 34 is easily computed to

$$s_{ii}=\frac{4\pi}{\lambda}A\sin\left(\frac{2\pi x}{\lambda}\right)\sin\left(\frac{2\pi y}{\lambda}\right), \tag{34}$$

and Eq. 34 is used to compute the error of s_{ii} as it is estimated by Method C. Figure 7 shows the mean bias and random error

$$\frac{1}{A\lambda^2}\int_0^{\lambda}\int_0^{\lambda}\left|E_{\mathrm{ph}}(s_{ii})-s_{ii}^{\mathrm{exact}}\right|\mathrm{d}x\,\mathrm{d}y, \tag{35}$$

$$\frac{1}{A\lambda^2}\int_0^{\lambda}\int_0^{\lambda}\sigma_{\mathrm{ph}}(s_{ii})\mathrm{d}x\,\mathrm{d}y, \tag{36}$$

respectively.

Regarding the total error levels of the measured displacement, Methods A and B are seen to achieve their best overall accuracy with the smallest interrogation window size 2R=16 px tested. The total overall displacement error of Method C is rather constant for 2R=16, 24 and 32 px, the larger of those producing more bias and less random

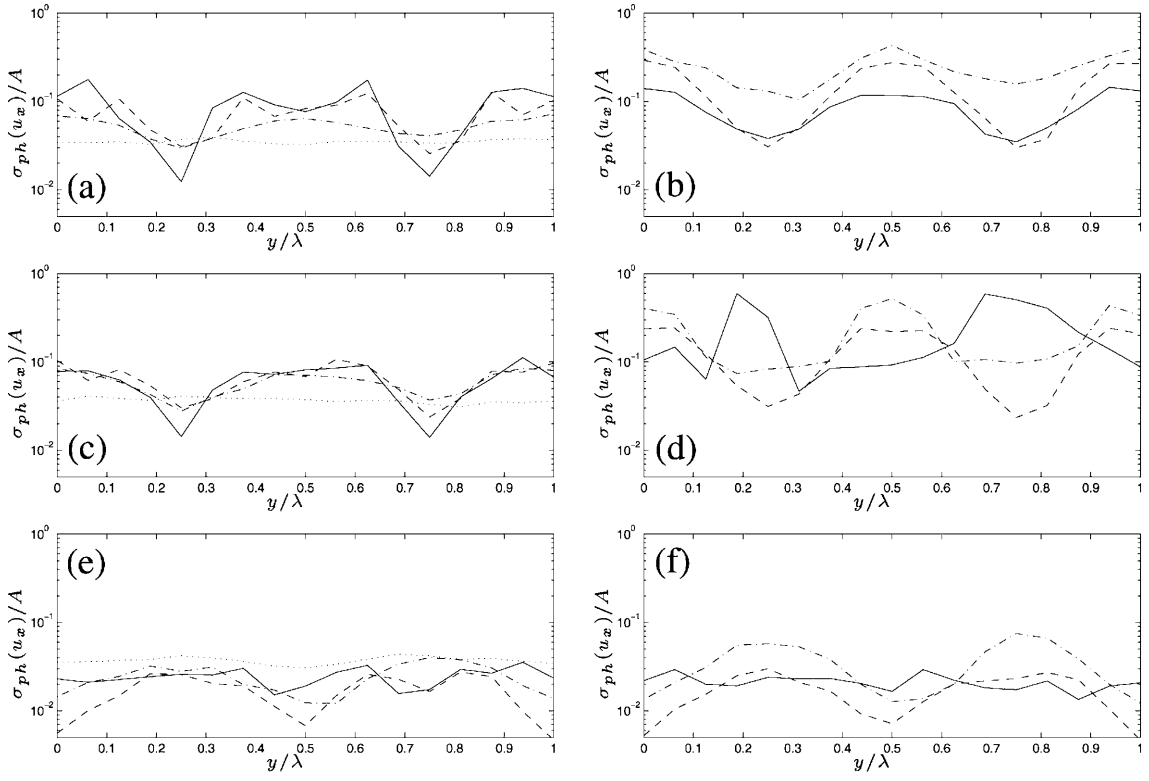

Fig. 5a–f. Synthetic PIV-image pair with periodic irrotational displacement field, Eq. 31 with particle image size d_p=4 px. Rms of phase-averaged velocity component along line x=0: **a** Method A, A=1 px; **b** Method A, A=5 px; **c** Method B, A=1 px; **d** Method B, A=5 px; **e** Method C, A=1 px; **f** Method C, A=5 px; —, $2R$=16 px; - - -, $2R$=32 px; ·-·, $2R$=64 px; · · ·, $2R$=128 px

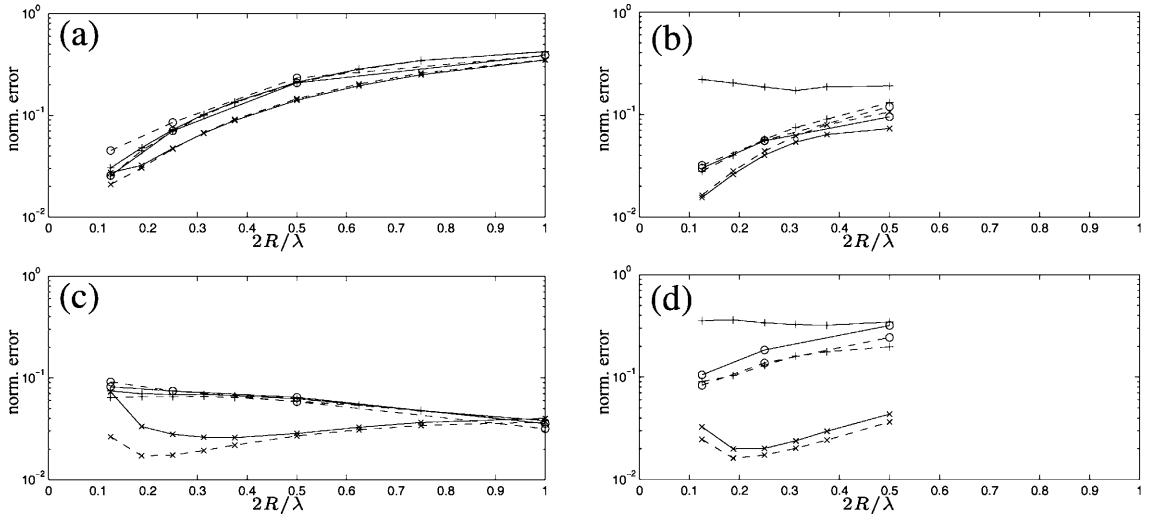

Fig. 6a–d. Synthetic PIV-image pair with periodic irrotational displacement field, Eq. 31. Mean of phase-averaged bias and random displacement errors averaged over one wavelength in either direction of the field: **a** norm. bias error, Eq. 32, A=1 px; **b** norm. bias error, Eq. 32, A=5 px; **c** norm. random error, Eq. 33, A=1 px; **d** norm. random error, Eq. 33, A=5 px; ❍, Method A; +, Method B; ×, Method C; —, particle image size d_p=2 px; - - -, particle image size d_p=4 px

errors and and vice versa. The total error of s_{ii} measured by Method C is seen to be smallest somewhere between $2R$=24 and 32 px.

3.3
Oseen vortex

The methods' capability of resolving a single vortex is investigated in a test similar to that of Huang et al. (1993) and others. Again a synthetic image pair is created by randomly distributing particles over the image plane of 1,024×1,024 px^2 with an average density of 0.0195 1/ px^2. The particles are displaced from one image to the other by an exact Oseen vortex with the center located at the image center and the angular displacement given as

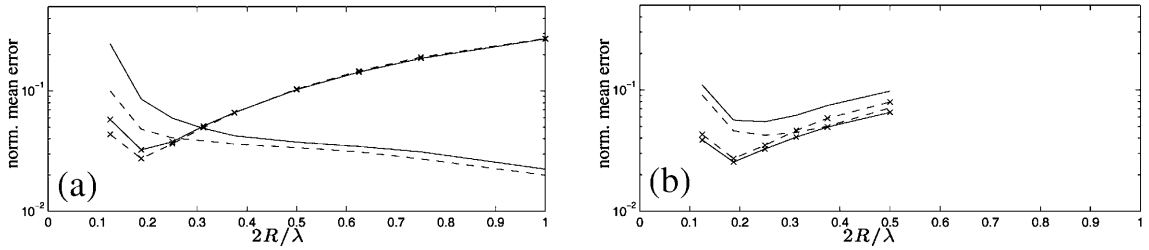

Fig. 7a, b. Synthetic PIV-image pair with periodic irrotational displacement field, Eq. 31. Method C. Mean of phase-averaged bias and random errors of divergence s_{ii} averaged over one wavelength in either direction of the field: **a** A=1 px; **b** A=5 px; -×-×-, norm. bias error, Eq. 35, d_p=2 px; - × -, norm. bias error, Eq. 35, d_p=4 px; —, norm. random error, Eq. 36, d_p=2 px; - - -, norm. random error, Eq. 36, d_p=4 px

$$V_\theta = \Lambda \frac{L^2}{r}\left[1 - e^{-\frac{1}{2}\left(\frac{r}{L}\right)^2}\right], \tag{37}$$

where L=115 px and Λ=0.1934 1/px, setting the vortex size to about 100 px and the maximum displacement in the field to 10 px. The vorticity of Eq. 37 can be computed to be

$$\Omega = \frac{1}{r}\frac{\partial r V_\theta}{\partial r} = \Lambda e^{-\frac{1}{2}\left(\frac{r}{L}\right)^2}, \tag{38}$$

and the only non-zero strain rate tensor element is

$$S_{\theta r} = \frac{r}{2}\frac{\partial}{\partial r}\left[\frac{V_\theta}{r}\right] = \frac{\Lambda}{2}\left[-\frac{L^2}{r^2} + \left(\frac{L^2}{r^2} + 1\right)e^{-\frac{1}{2}\left(\frac{r}{L}\right)^2}\right]. \tag{39}$$

This test features a maximum displacement gradient of about 20% in the vortex core, while the maximum magnitude of the second displacement derivative is seen at a distance of about 100 px from the vortex center to be about 10^{-3} 1/px.

Again every particle is projected onto the discrete images with a Gaussian bell intensity distribution of the sizes d_p=2 px and d_p=4 px, respectively. Additionally, 10% white noise is added to each image.

Figures 8 and 9 show the error of the length of the velocity vector compared with the exact profiles as a function of the distance r from the vortex center point. Methods A and B are seen to yield similar results, although random error levels overall are a little lower for Method B. In the vortex core region, the random error component tends to grow with increasing window size for both methods, while it decreases in the vortex periphery. Using larger interrogation windows, some negative bias error can be detected additionally in the vortex core region. Using Method C, the error dependency on the interrogation window size is fundamentally different. For 2R=16 px, see Fig. 8c, the average error is not larger than in Methods A and B; however, in a few windows outlier values are produced. As before, increasing the window size removes such outliers everywhere in both the vortex core and in its periphery and further increase in the window size further reduces the random error component. Also, Method C produces some limited bias error when using larger windows, although clearly less than Methods A and B. Not being shown, the

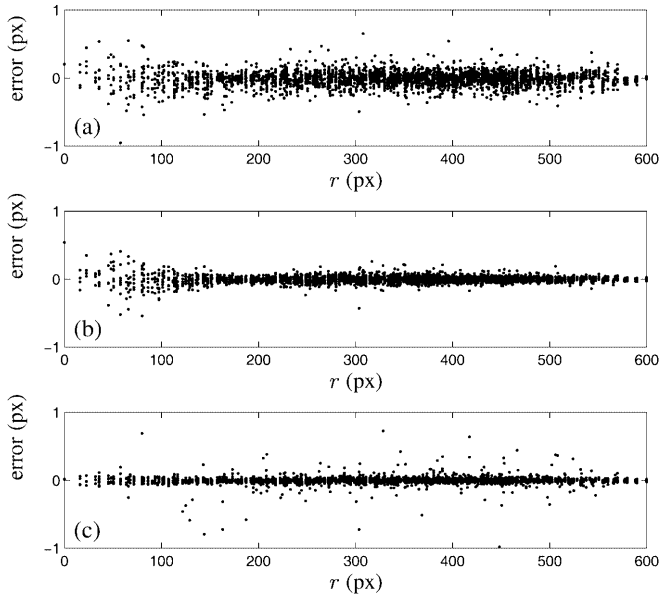

Fig. 8a–c. Synthetic PIV-image pair of Oseen vortex. Particle image size d_p=4 px. Tangential displacement error $|(u,v)|-V_\theta$ for every window as a function of distance r from vortex center. Interrogation window size 2R=16 px: **a** Method A; **b** Method B; **c** Method C

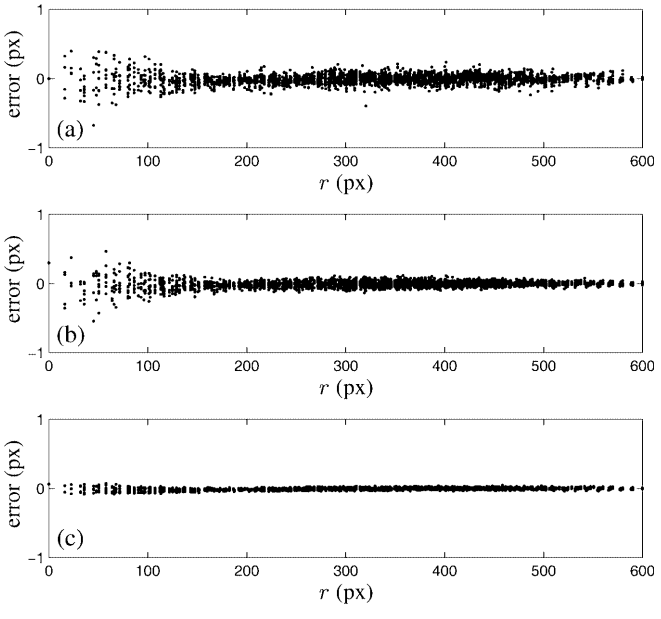

Fig. 9a–c. Synthetic PIV-image pair of Oseen vortex. Particle image size d_p=4 px. Tangential displacement error $|(u,v)|-V_\theta$ for every window as a function of distance r from vortex center. Interrogation window size 2R=32 px: **a** Method A; **b** Method B; **c** Method C

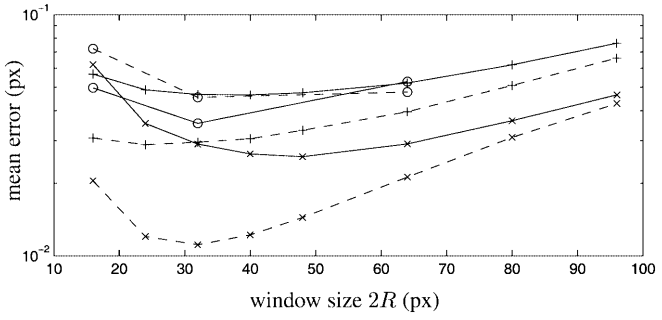

Fig. 10a–c. Synthetic PIV-image pair of Oseen vortex. Displacement error $|(u,v)|-V_\theta$. Comparison of average error made by different analysis methods as a function of interrogation window width: ❍, Method A; +, Method B; ×, Method C; —, d_p=2 px; - - -, d_p=4 px

errors of the velocity angle are considerably larger for Methods A and B than for Method C, in particular in the vortex core region. Its dependency on window size follows the tendency of the velocity norm error. Further, the standard approach (Method A) produces asymmetric velocity fields, seen by a significant bias of the velocity angle profile.

For all three methods, the vorticity is estimated by central differences in the displacement components,

$$\omega_{\mathrm{FD}}(x,y)=\frac{v(x+\Delta,y)-v(x-\Delta,y)}{2\Delta}-\frac{u(x,y+\Delta)-u(x,y-\Delta)}{2\Delta}, \tag{40}$$

the step size being Δ=16 px. Figure 10 shows the normalized error, when compared with Eq. 38, Method C having random errors one order of magnitude smaller than the other two methods. With Method C, additionally to finite difference approximations, the vorticity is estimated directly. Figure 11 shows the average error of the normalized vorticity for different interrogation window sizes as a function of the distance from the vortex center point. Using $2R$=16 produces very significant scatter; however, larger windows again narrow the noise level in the estimation, yielding considerable accuracy.

In Fig. 12, total displacement errors are averaged over the field and plotted as function of interrogation window size for the three methods. Methods A and B provide their optimum somewhere between $2R$=24 px and 32 px, while Method C yields minimum error levels at $2R$=32 px and $2R$=48 for the particle image sizes d_p=4 px and d_p=2 px, respectively. Contrary to the standard method, the methods based on optimization clearly produce least errors for the largest particle image size, tested. Apart from the case of $2R$=16 px and d_p=2 px, Method C performs generally better than the other methods.

Figure 13 shows the average error of the measured vorticity, divergence, and shear rate as computed by Method C for different window sizes. It is noteworthy that the least total error is produced with a window as large as $2R$=92 px.

4 Discussion

In Sect. 3, an attempt has been made to demonstrate the properties of the new method and to compare the results

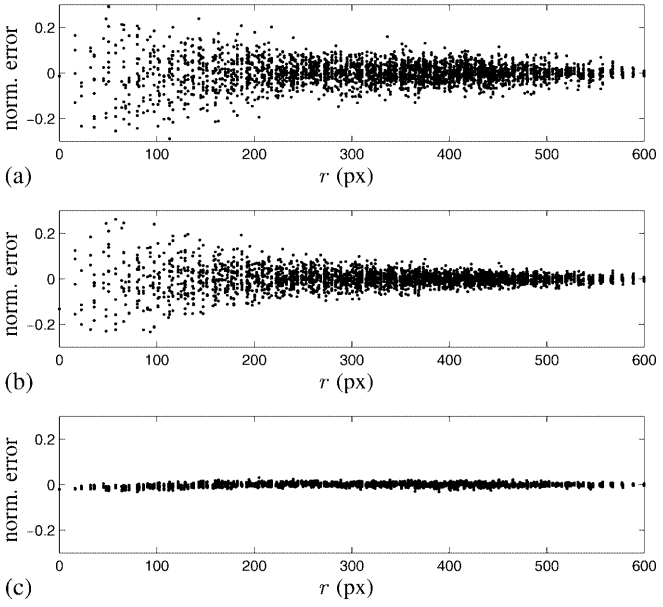

Fig. 11a–c. Synthetic PIV-image pair of Oseen vortex. Normalized vorticity error $(\omega-\Omega)/(\Lambda)$ for every window as function of distance r from vortex center. Vorticity is computed by central differences. Interrogation window size 32 px: **a** Method A; **b** Method B; **c** Method C

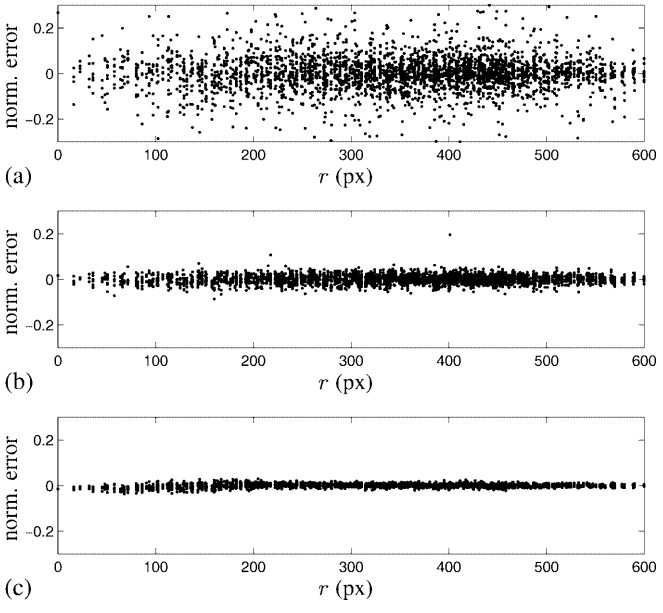

Fig. 12. Method C, optimization of $q=(u,v,s_{ij})$ on synthetic PIV-image pair of Oseen vortex. Normalized vorticity error $(\omega-\Omega)/(\Lambda)$ for every window as function of distance r from vortex center: **a** $2R$=16 px; **b** $2R$=32 px; **c** $2R$=64 px

with the standard approach. In the following, results are discussed and their implications outlined. Effectively, the comparison procedure is divided into two parts: first the effect of the collocation method itself is tested with linear displacements only (Method B) and compared with the standard approach. Secondly, the influence of taking into account displacement gradients into the interrogation procedure (Method C) is tested. The MatPIV package (Method A) was used as the standard method, because it is readily available.

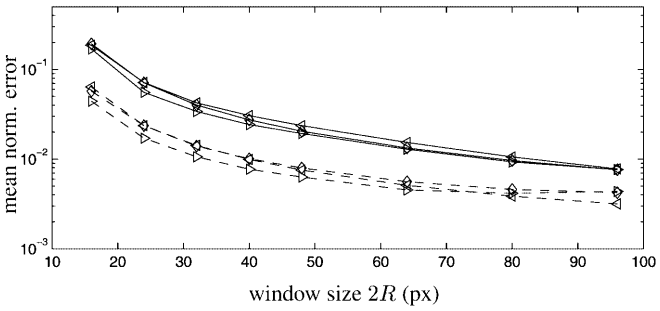

Fig. 13. Method C, optimization of $q=(u,v,s_{ij})$ on synthetic PIV-image pair of Oseen vortex. Comparison of average total error of differential quantities as function of interrogation window width $2R$: *diamonds*, vorticity error, $(\omega-\Omega)/(\lambda)$; *left triangle*, divergence error, $s_{ii}/(\alpha\lambda)$; *right triangle*, shear rate error, $\left(\sqrt{S_{ij}S_{ij}}-\sqrt{2}(S_{\theta r})/(\Lambda)\right)$; *continuous lines*, d_p=2 px; *dashed lines*, d_p=4 px

It is a requirement for being able to extend the usual discrete shifting operator to the image distortion with affine transformations that the processed images are treated as continuous functions at least partly in the process. In the image-distortion approaches of Huang et al. (1993), Huang (1998), Jambunathan et al. (1995) and Nogueira et al. (1999), affine transformation of the images is used only for re-sampling, while interrogation still relies on the usual discrete FFT-based cross-correlation analysis. In contrast, the present method window integrates image distortion directly into the interrogation procedure without need of pre- and post-processing. The problem of the in-plane losses of particle pairs (usually solved by interrogation window shifting) has a simple straightforward solution in the new method, since the affine transformation of the collocation points shifts the interrogation window automatically in either image in both location and shape. Since the images are correlated at the virtual time t_h, where the shifted collocation points coincide, the two image patterns are easily compared.

A second major difference is the implementation of the correlation function by use of collocation points. Once the images are transferred from the discrete index space (i,j) into continuous coordinates (x,y), full freedom is given in the choice of interrogation window shape. Theoretically, as much symmetry as possible in time as well as in space should be introduced in the interrogation procedure. Therefore, we believe the circular shape to be the best choice. Due to the affine transformation of collocation points x_i in either direction, given by $\pm q/2$, the velocity field is a second-order approximation to the velocity field at time $t_h=(t_1+t_2)/2$, preserving symmetry as seen in Figs. 4.

A further difference can be seen in the fact that, since the new method does all analysis in the continuous space (x,y), the results are by definition continuous and therefore further sub-pixel interpolation around the correlation peak is not needed.

In the present investigation based on synthetic images, a number of real-life error sources such as electronic noise, inhomogeneous seeding and light sheet, out-of-plane loss of particles, etc. have been neglected. The remaining errors are essentially due to the discretization to pixelized images and due to the non-uniformity of the displacement field. The size of errors in the tests is generally determined by the following three parameters: First, the average number of particles within an interrogation window determines the amount of information on the basis of which measurements are made within a window. Secondly, the relative size of the interrogation window compared with the length scale of the displacement gradients in the field determines the difference of particle displacements within the window, and the resulting broadening of the correlation peak. The third parameter is the particle image size, determining the size of the discretization error and the width of the correlation peak. In order to save computational time for the tests and to reduce the amount of data to be presented, only the particle image size and the window width were varied in the present study. The particle density was kept constant, making the number of particles within the window proportional to the window area.

4.1 Random errors

The random errors produced by the three methods are primarily determined by the number of particles within a window and by the broadening of the correlation peak due to displacement differences within the window. Random errors in PIV are generally known to grow with decreasing number of particles within a window, which is confirmed by the present results. Given only a limited number of particles, Method C suffers more than the other methods, because more information is required to determine six parameters $q=(u, v, s_{11}, s_{22}, s_{12})$ than only two (u, v). Theoretically, at least three particles are necessary in either image to determine q uniquely, while one particle is sufficient in the standard method and Method B. This effect can be seen in the present study when using the window size $2R$=16, since the average particle density used in the test corresponds to an average of 3.9 particles per window, being close to the theoretical limit.

Hence, in PIV the signal-to-noise ratio is increased by increasing the window size due to the increased number of particles within a window, as long as displacement differences within the window do not broaden the correlation peak. Broadening of the peak in Methods A and B begins when those displacement differences grow to scales similar to the average particle image size. In such cases, the random error component of standard PIV is known to increase considerably. In Method C, the correlation peak does not broaden as long as an inherent first-order Taylor expansion is a good approximation to the displacement field over the window area. Hence, unlike Methods A and B, the signal-to-noise ratio of Method C still further increases when enlarging the interrogation window. This behavior is similar to that reported for the window distortion techniques (see e.g., Huang et al. 1993; Scarano and Riethmuller 2000) and the growth of the signal-to-noise ratio is continued as long as higher-order velocity derivatives can be neglected. This is demonstrated in Fig. 5, Method C having the highest random errors where second-order displacement derivatives have their maximum, while both Methods A and B show maximum noise-levels at

locations with maximum first-order derivatives in the displacement field. At such locations Method C produces least noise, since here the second-order displacement derivative vanishes due to the sinusoidal profile of Eq. 31.

It is well known in the PIV literature that finite difference approximations of measured velocity vectors suffer from the large random errors present in the velocity estimates, see e.g., Raffel et al. (1998). This is the reason for usually employing other numerical differentiation schemes and various smoothing algorithms, to some extent reducing spatial resolution. Since the random errors of Method C are reduced, finite differences can be employed with considerably higher accuracy (see Fig. 10). At first view, surprisingly, the error in the directly estimated vorticity (Fig. 11b) is considerable larger than that found by finite differences (see Fig. 10c), using the same interrogation window width. However, using $2R$=64 yields errors which are comparable with the ones obtained by finite differences of the velocity components found with $2R$=32. This indicates that the directly estimated gradients are equivalent in accuracy to finite difference approximations, as long as the area of the PIV image used for the estimation is similar.

4.2
Bias errors, peak-locking and spatial resolution

With the use of interpolation in the pixel space of the image, errors in the velocity estimates arise, similar to the errors introduced by sub-pixel interpolation within the standard PIV framework, usually termed peak-locking. Considerable bias errors are introduced by the bilinear interpolation in Methods B and C, the errors being largest for small particle image sizes. The peak-locking effect in the standard method is virtually removed in the constant displacement test, since the Gaussian sub-pixel interpolation scheme is constructed for the Gaussian intensity distributions of the synthetic particles images used in the tests. However, even in the weak case (A=1 px) of the irrotational oscillatory field (see Fig. 6), the bias error produced by the standard method is dependent on the particle image size, the dependency in fact being of the same order of magnitude as that of Methods B and C. This is so because the correlation peak in Method A is no longer of Gaussian shape due to displacement differences within the window, despite the Gaussian profiles of individual particle images.

It should be pointed out that peak-locking effects similar to those of Method C have to be expected for the image distortion techniques in the literature, since they all use bilinear interpolation in the re-sampling procedure of the distorted second image. However, once displacement gradients are taken into account by either image distortion or within the pattern matching algorithm itself, such bias errors prove to be less disturbing in the measurement of strained flows. This is because the peak-locking effect is local to each particle in the window and is to some extent averaged out if particles within the window have different sub-pixel displacements. However, is is still worthwhile to consider other interpolation techniques, such as, for example, higher-order piecewise interpolation methods or splines, such option having been investigated by Fincham and Delerce (2000) and Scarano and Riethmuller (2000), for example.

The spatial resolution of all the methods is restricted by the Nyqvist limit, since velocity fluctuations on the scale of the interrogation window are averaged out in the measurement. Introducing displacement gradients in the interrogation procedure does not remove that limit. Similar to what is shown in Nogueira et al. (1999) and Scarano and Riethmuller (2000), the ability of spatially resolving details in the displacement field can be described by defining a spatial wavelength response function. Based on the oscillating displacement test in the present study, a response function is defined by finding the maximum phase-averaged x displacement $E_{\mathrm{ph}}(u_x)$ at $(x,y)=(0,\lambda/4)$ (see Fig. 14). For all three methods tested, the response is essentially that of a sliding average over the window area, as expected. While the response of the standard method is practically identical to that of a sliding average with constant weight, Method B is slightly less damping due to its non-constant weighting function $w(r)$ and effectively smaller, circular window shape. Method C shows the least damping properties, having an amplitude reduction half that of the sliding average as long as the window size is less than half the oscillation wavelength.

4.3
Application to real experimental image pairs

Westerweel (2000) and others have pointed out that the testing of PIV processing algorithms with synthetically produced image data can give very optimistic estimates of a method's capabilities. Further, in the present study not only the method's accuracy, but also its robustness has to be demonstrated with respect to real experimental images, since the method relies on gradient-based optimization – a technology that is prone to convergence problems. It is beyond the scope of the present paper to investigate such aspects thoroughly. Here, only a demonstration is given of the differences which can be expected between the results of the standard procedure and the present method. To accomplish this, an image pair from Ullum (2000) is processed with turbulent boundary layer air flow behind a fence. The nominal Reynolds number based on the fence height h=40 mm is Re_{h}=1300 and the pixel width corre-

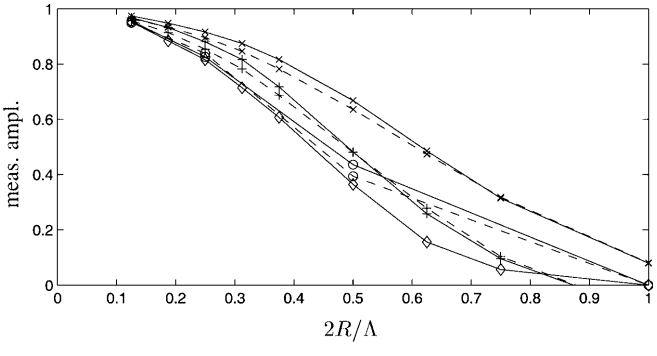

Fig. 14. Synthetic PIV-image pair with periodic irrotational displacement field, Eq. 31, A=1 px. Amplitude of measured x-displacement as function of relative window width: ◇, moving average; ○, Method A; +, Method B; ×, Method C; —, d_{p}=2 px; - - -, d_{p}=4 px

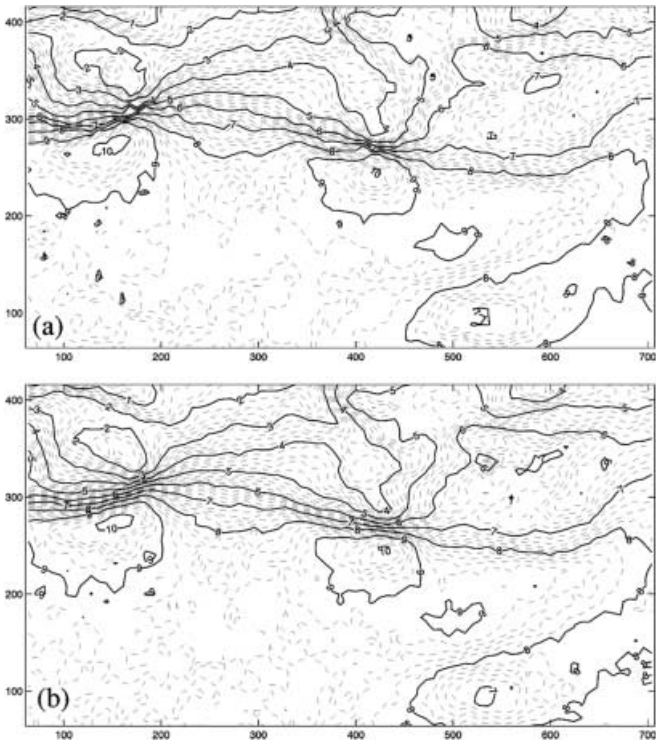

Fig. 15a, b. Speed of flow behind fence. Interrogation window size $2R$=16 px: **a** Method A; **b** Method C

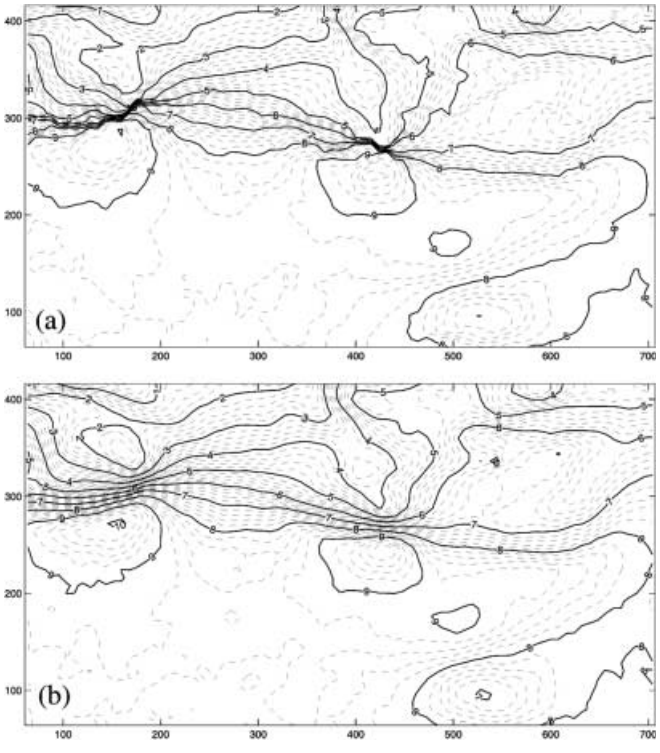

Fig. 16a, b. Speed of flow behind fence. Interrogation window size $2R$=32 px: **a** Method A; **b** Method C

sponds to $px=1.8\times10^{-3}h$. The time interval between the two images was adjusted to give maximum particle displacements in the field of about 10 px. The tracer is spray of a mix of water and glycerol, yielding particles of diameter between 1 and 3 μm. The images were preprocessed by subtracting from the image a local mean pixel intensity that was found by sliding averages over an 11×11-px^2 area. All three methods are applied to the image pair for different interrogation window sizes.

Figures 15 and 16 show the norm of the displacement vector, as computed for the window size $2R$=16 px and 32 px by Methods A and C. The results of Method A is overall very similar to that of Method B (not shown): for small interrogation windows, many similar details are resolved and the quality of the measurement seems to be equivalent. For larger windows, the velocity field appears to be smoothed, which is expected due to the filtering effects of the local averaging within each window, reducing local extremum velocity values. However, in some isolated parts of the plane, local strong gradients seem to be amplified, such a discontinuous response being reported by others (see e.g., Scarano and Riethmuller 2000). Method C, in contrast, appears to provide a more detailed but smoother velocity field than the other methods, using similar window sizes. Further, the use of larger interrogation windows appears only to have a smoothing effect also in the strong gradients regions mentioned, with the qualitative features of the velocity field in all cases being retained.

4.4
Choice of objective function

Since the correlation operator C is computed using direct summation, it could be substituted with any other objective function expressing similarity of two image patterns. AsFincham and Delerce (1997) and Huang et al. (1997), for example, have pointed out, the correlation operator should be substituted with the covariance operator, being normalized with respect to the average pixel intensity and intensity variance of either of the two patterns to be matched. By this normalization, the interrogation algorithm becomes less sensitive to spatial gradients in the images that are caused by inhomogeneous light sheet intensity, inhomogeneous particle seeding, etc. Accordingly, Eq. 25 could be substituted with

$$C(F_1,F_2)=\frac{1}{N}\sum_i \frac{[w(r_i)F_1(x_i,y_i)-E(F_1)][w(r_i)F_2(x_i,y_i)-E(F_2)]}{\sqrt{V(F_1)V(F_2)}} \tag{41}$$

where E and V denote the mean and variance operators, respectively

$$E(F)=\frac{1}{N}\sum_i w(r_i)F(x_i,y_i), \tag{42}$$

$$V(F)=\frac{1}{N}\sum_i [w(r_i)F(x_i,y_i)-E(F)]^2. \tag{43}$$

Preliminary tests using Eq. 41 do not show any significant changes in the results for any of the examples in the present paper. Generally, random errors are slightly larger than with Eq. 25 in use. Further, the optimization algorithm on average needs a few more iterations, resulting in a minor loss of computational efficiency. However, the

synthetic images used for the present testing are obviously very clean, so no final conclusion can be drawn at present. Another possibility worth testing is the MQD approach of Gui and Merzkirch (2000), also being easily implemented within the current framework.

Nogueira et al. (1999) reports that the image distortion technique of Huang et al. (1993) suffers from numerical instabilities when used iteratively. Nogueira et al. (1999) ascribe this unstable behavior to the spatial frequency response of standard PIV interrogation methods, being negative for certain spatial frequencies, and they showed that removing the negative response by introducing weight function in the cross-correlation operator removes the instabilities. Also, the present method uses a weight function in the correlation operator. However, the frequency response does not determine the stability of the method, since an implicit optimization method is employed, while the image distortion procedures are essentially explicit, image distortion being dependent on displacement fields measured at previous iterations. The primary function of the weighting function in the present approach is to guarantee reasonable smoothness of $G(q)$, since the optimization routine VF13AD formally requires both $G(kq)$ and $\frac{\partial G(kq)}{\partial kq}$ to be continuous. In the case $w(r_i)=1$ for all collocation points (x_i,y_i), small changes of q could imply abrupt changes in G when moving the window over a particularly bright spot in the image. Giving low weights to the periphery of the window reduces this tendency.

4.5
Robustness of the method

In all correlation-based PIV analysis, the location of the maximum correlation is sought in one way or another. In the standard PIV method, fast algorithms are used for the calculation of the image cross-correlation, making it feasible to cover the whole relevant parameter space (u,v) with only a moderate computational burden. The location of the maximum correlation is then determined by a simple search algorithm. However, in order to find the correlation peak, it is not necessy to compute values for the cross-correlation for a large sample of (u,v), as long as the region around the correlation peak is well resolved. Usually in general optimization problem solving, search procedures would be avoided and instead more intelligent techniques are employed to track down an optimum with as few evaluations of the objective function as possible. The drawback of this approach compared with the use of search algorithms is that the objective function must be smooth and usually must have smooth gradients. Further, convergence of the method cannot be guaranteed, and no warranty can be given that the optimum found is global, if local optima exist. In gradient-based optimization, the easier it is to solve the problem, the smoother is the objective function to be minimized. Hence the correlation analysis of tracer scalar fields, as in Tokumaru and Dimatakis (1995) and others, is particularly easier, as in the present case, where the correlation function is only smooth within scales of the average particle image size, and the correlation optimum is searched locally without any additional smoothness constraints. However, due to the usually good starting guess available, typically it would locate the global peak within 10–20 iteration steps to the required convergence criterion. Most of the iteration steps are spent in the process of finding the approximate location of the optimum. When the peak has eventually been identified, the subsequent exact pinpointing of the peak location within sub-pixel accuracy is always obtained within a few iteration steps. The convergence behavior does not appear to be very sensitive to the interrogation window size, as long as there is a sufficient number of particles within the window, but it is obviously very dependent on good starting guesses.

The production of outliers in the processing of the synthetic image pairs is generally due to either of two reasons. In cases with fewer than three particles within a virtual window, clearly a correct correlation optimum cannot be found. The method would then either converge into a peak due to noise or would shift the window in either of the images, so that the image patterns within the transformed windows $S_{\frac{1}{2}\pm kq}(p_h)$ in either image, I_1 and I_2, respectively, feature three particles. The location q of the optimum will obviously be wrong; however, the correlation peak found will usually be quite high. The second reason for outlier production comes into effect in cases where the transformation S_q is an inaccurate approximation of the displacement field within A. This results in a broadening of the correlation peak in such a way that the optimization algorithm might converge within arbitrary weak local optima. This is easily detected, since unlike the former case, the correlation peak found is weak. Since the width of the correlation peak in the kq-parameter space is essentially of the order of the average particle image size, the problem of outlier production increases with decreasing particle image size.

4.6
Computational efficiency

The main workload in the optimization procedure lies in the evaluation of the correlation $G(kq)$, which on a typical year-2000 PC (800 MHz AMD Athlon) is timed to require $10^{-5}N$s, N being the number of collocation points used. Assuming 10–20 iteration steps to be necessary, every step requiring seven evaluations of $G(kq)$, the typical processing speed is about five windows per second for a window size of $2R=16$ px. This efficiency is clearly inferior to the speed of a standard method. However, if the point of view is somewhat similar to the philosophy of Fincham and Spedding (1997and Fincham and Delerce 2000), requiring accuracy regardless of the computational cost, the computational overhead of the present method is certainly acceptable. Further, it should be noted that once the location of the correlation peak has been determined for one interrogation window size, it usually only costs one to three iterations to find the peak location for another slightly different window size, due to the very good starting guess available. In this way, only moderate additional costs are generated by computing results for a whole cascade of interrogation window sizes. The additional data can give valuable additional information, for example when attempting to demodulate the averaging effect of the

PIV interrogation in order to improve spatial resolution, as proposed by Scarano and Riethmuller (2000).

From a numerical and implementational point of view, quite some possibilities of improving the efficiency of the present method can be imagined. An attempt should be made to avoid the calculation of a full Jacobian in the optimization algorithm, since it in the present implementation accounts of more than 50% of the total computation time. As often done in similar iterative algorithms, the Jacobian could be reused to some extent from former steps, or Broyden updates to the Jacobian could be employed, only requiring one additional evaluation of the objective function. Further, parallelization of the interrogation algorithm is trivial due to its very local nature.

5 Conclusion

In the present study, a new method is presented for the processing of PIV image pairs. It integrates previous suggestions on how to take into account particle displacement gradients in a simple consistent technique. It also solves the problem of sub-pixel interpolation in a straightforward manner, gives full freedom in the choice of interrogation window geometry, and solves the problem of in-plane loss of particle pairs without any further processing.

By applying the new method to synthetic sample image pairs, it is demonstrated that the method (similar to window distortion techniques) can improve measurement accuracy considerably by reducing the random error levels usually encountered when measuring strongly strained flow and by providing a somewhat less damping wavelength response to local flow features. Hence the dynamic range of measurements of velocity gradient, i.e., vorticity, is significantly enhanced. In its present state, the computational cost of the method is higher than that of the conventional approach.

The present study only documents the first test with this new method, and many different aspects need further investigation. In particular, how real life error sources such as electronic noise, out plane loss of particles, varying particle image sizes, very high particle densities, inhomogeneous particle seeding and light sheet intensity, etc. affect the measurements must be tested.

References

Deusch S, Merava H, Dracos T, Rys P (2000) Measurement of velocity and velocity derivatives based on pattern tracking in 3d LIF images. Exp Fluids 29:388–401

Fincham A, Spedding G (1997) Low cost, high resolution DPIV for measurement of turbulent fluid flow. Exp Fluids 23:449–462

Fincham A, Delerce G (2000) Advanced optimization of correlation imaging velocimetry algorithms. Exp Fluids 29:S13–S22

Fouras A, Soria J (1998) Accuracy of out-of-plane vorticity measurements derived from in-plane velocity field data. Exp Fluids 25:409–430

Gui L, Merzkirch W (1998) Generating arbitrarily sized interrogation windows for correlation based analysis of the particle image velocimetry recordings. Exp Fluids 28:66–69

Gui L, Merzkirch W (2000) A comparative study of the MQD method and several correlation based PIV evaluation algorithms. Exp Fluids 28:36–44

Huang HT (1998) An extension of digital PIV-processing to double exposed images. Exp Fluids 24:364–372

Huang HT, Fiedler HE, Wang JJ (1993) Limitations and improvement of PIV, Part II. Particle image distortion, a novel technique. Exp Fluids 15:263–273

Huang HT, Dabiri D, Gharib M (1997) On errors of particle image velocimetry. Meas Sci Technol 8:1427–1440

Jambunathan K, Ju X, Dobbins B, Ashforth-Frost S (1995) An improved cross correlation technique for particle image velocimetry. Meas Sci Technol 6:507–514

Jensen A, Sveen J, Grue J, Richon J, Gray C (2001) Accelerations in water waves by extended particle image velocimetry. Exp Fluids 30:500–510

Lin H, Perlin M (1998) Improved methods for thin, surface boundary layer investigations. Exp Fluids 25:431–444

Madsen K, Tingleff O, Hansen PC, Owczarz W (1990) Robust subroutines for nonlinear optimization. Technical Report NI-90-06, Institute for Numerical Analysis, Technical University of Denmark

Merkel G, Rys P, Rys F, Dracos TA (1996) Concentration and velocity field measurements in turbulent flows using laser-induced fluorescence tomography. Appl Sci Res 56:181–190

Nogueira J, Lecunona A, Rodriguez P (1997) Data validation, false vectors correction and derived magnitudes calculation on PIV data. Meas Sci Technol 8:1493–1501

Nogueira J, Lecunona A, Rodriguez P (1999) Local field correction PIV: on the increase of accuracy of digital PIV systems. Exp Fluids 27:107–116

Powell M (1982) Extension to subroutine vf02ad. In: Lecture notes in control of informatics sciences, vol 38. Springer, Berlin Heidelberg New York, pp 529–538

Raffel M, Willert C, Kompenhans J (1998) Particle image velocimetry: a practical primer. Springer, Berlin Heidelberg New York

Scarano F, Riethmuller M (1999) Iterative multigrid approach in PIV image processing with discrete window offset. Exp Fluids 26:513–523

Scarano F, Riethmuller M (2000) Advances in iterative multigrid PIV image processing. Exp Fluids 29:S51–S60

Tokumaru P, Dimatakis P (1995) Image correlation velocimetry. Exp Fluids 19:1–15

Ullum U (2000) Image techniques for planar velocity and concentration measurements. Ph.D. Thesis, Department of Energy Technology, Technical University of Denmark

Westerweel J (2000) Theoretical analysis of the measurement precision in particle image velocimetry. Exp Fluids 29:S3–S12

Westerweel J, Dabrii D, Gharib M (1997) The effect of a discrete window offset on the accuracy of cross-correlation analysis of digital PIV recordings. Exp Fluids 23:20–28